Activated zirconium carbide promoted Pt/C electrocatalyst for oxygen reduction

CrossMark

P. Justin [a,b], P. Hari Krishna Charan [a], G. Ranga Rao [a,*]

[a] Department of Chemistry, Indian Institute of Technology Madras, Chennai 600036, India
[b] Department of Chemistry, Rajiv Gandhi University of Knowledge Technologies, RGU IIIT, RK Valley Campus, Andhra Pradesh 516329, India

ARTICLE INFO

ABSTRACT

The activated porous zirconium carbide (ZrC) is prepared by sodium carbonate activation of commercial ZrC. As a result of sodium carbonate activation, there is a tremendous increase in the surface area (from 0.6 to 96 $m^2 g^{-1}$) and chemisorption capability of commercial ZrC. This ZrC is incorporated into Vulcan carbon XC-72R by solid-state reaction using intermittent microwave heating (IMH) method, and Pt nanoparticles were dispersed by microwave-assisted polyol process. The electrocatalyst samples were characterized by PXRD, BET, SEM, TEM, XPS and their performance for oxygen reduction reaction was studied in 0.1 mol L^{-1} $HClO_4$ aqueous electrolyte by cyclic voltammetry and rotating ring disk electrode. The XRD, XPS and TEM results indicate well dispersed ZrC and Pt nanoparticles over Vulcan carbon XC-72R. When the activated ZrC combined with platinum, the resulting composite electrocatalyst showed higher activity for oxygen reduction which exceeds that of the commercial Pt/C catalyst of similar metal loading. Our approach shows that sodium carbonate activation is an effective method for the activation of metal carbides, which is essential for tuning the microstructural properties of electrocatalyst support.

1. Introductin

Catalysts for oxygen reduction reaction (ORR) play a very crucial role in low temperature fuel cells, especially in proton-exchange membrane fuel cells (PEMFCs) and direct methanol fuel cells [1–8]. The reduction of dioxygen by four electrons is the most attractive reaction to catalyze, as it gives highest cell voltage for a fuel cell. Even the best catalyst, Pt, is at least 10^6 times less active for oxygen reduction than for H_2 reduction or H_2 oxidation ($i_0 = \sim 10^{-3} A cm^{-2}$). Poor kinetics of oxygen reduction leads to more than 0.3 V voltage loss under reasonable operating currents [3]. In the mechanism, the formation of the two-electron reduction product, H_2O_2, will reduce the effective electron-transfer number of the ORR. Thus the efficiency of fuel cells is limited on the cathode side by the ORR in terms of both the mechanism and its kinetics [8]. The research is mainly focused on two aspects, either to minimize the Pt content or to use Pt-free compounds to address this problem. The alloying of Pt with other transition metals like V [9], Cr [10,11], Fe [12], Co [3,13,14], Ni [15] and Cu [16] improved the kinetics of oxygen reduction and proved to be cost effective. Among various Pt-based transition metals binary alloy catalysts, Pt-Co catalytic system has been studied extensively because it exhibits almost 2–3 times higher mass-based activity compared to pure Pt [3]. The

enhanced electrocatalytic activity of binary alloy catalysts, in general, is explained by many ways which include shortened Pt–Pt bond distance, reduced sintering rates, increased surface roughening, decreased adsorption of anions and oxygen species. However, this class of catalysts suffered from dissolution of non-noble compound into the membrane under acidic conditions, especially at high voltages (pH $\approx$ 0, E = 0.8–1.1 V vs RHE) resulting in fast degradation. This makes them vulnerable in fuel cell applications at higher voltages [13]. But some well ordered Pt–M alloys are found to be more stable under these conditions than the constituent metals. For example, Pt is reported to leach into the membrane more easily from pure Pt than Pt alloys such as Pt_3Cr and PtCo [3,10].

The non-Pt catalysts, typically Pd alloyed with other elements such as Fe [17,18], Co [19], Cu [20], Ti [6] and W [21] have also been found to increase the ORR activity significantly compared to pure Pd. In this approach Pt is avoided but it results in considerable shift of onset potential in the negative direction. However, the Pd based catalysts are more tolerant for methanol and therefore can be considered to be possible replacement for Pt in the cathodes of DMFCs [21,22]. In a recent work Pd-Pt nanodendrites are shown to be two and half times more active for the ORR than the Pt/C catalyst on the basis of equivalent Pt mass [23]. Hence it is highly desirable to find ORR catalysts that are not only more active than Pt but also free from precious metals. A few classes of materials have been identified as noble metal free catalysts for ORR [24–30]. Pyrolyzed Fe and Co macrocycles [24,25], chalcogenides based on Co, Ru, Re, or Rh [1,26,27] and metal carbides [28–31] have been investigated as

* Corresponding author. Tel.: +91 44 2257 4226; fax: +91 44 2257 4202.
E-mail address: grrao@iitm.ac.in (G.R. Rao).

non-precious metal systems for ORR. The other interesting material is the porphyrin N_4-macrocycles ring system, which activates the O—O bond in natural environments, but does not have direct application in fuel cells in this form. However its derivatives with Fe or Co as central ions show some activity and durability in fuel cell applications [24,32]. Recently, the cobalt-polypyrrole composite cathode catalyst enables power density of about 0.15 W cm^{-2} for H_2-O_2 fuel cells, and displays no sign of degradation in performance for more than 100 h [7]. One problem associated with this promising catalyst system is the *overpotential* (0.15–0.20 V) of ORR in the low-current density region, which should be brought down closer to that of the Pt and Pt-based cathode catalysts.

Another approach is to use Pt nanoparticles on different catalyst supports since it is known that the support may significantly affect the catalyst performance or by tailoring the Pt particle size to control the relative fraction of Pt surface atoms. These strategies can significantly improve the electrode performance for ORR in terms of enhanced activity and poison resistance. Transition metal carbides, especially tungsten carbide, have been investigated as CO tolerant cathode catalysts which showed good corrosion resistance, high electrical conductivity and Pt like behavior for the chemisorption of hydrogen and oxygen [28–31]. Metal carbides seem to be promising for ORR due to synergetic effects between Pt and carbides. Recent work by Sampath and his coworkers on TiC clearly shows superior activity of TiC nanostructures compared to bulk TiC for the ORR in alkaline media. These authors also demonstrated the shape-dependent electrocatalytic activity of TiC nanostructures involving approximately 4 electron reduction of molecular oxygen. In this present work, porous ZrC is prepared by sodium carbonate activation of commercial ZrC and evaluated it as a co-catalyst to Pt/C for ORR. The activated ZrC-Pt composite electrocatalyst showed higher activity than the commercial Pt/C catalyst for ORR.
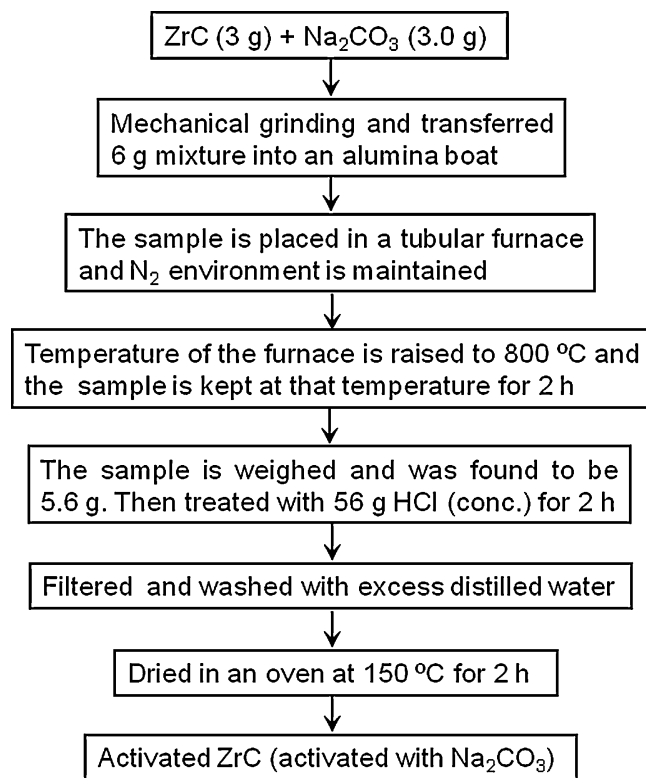
2. Experimental

2.1. Activation of commercial ZrC

The commercial ZrC (Material Research Corp., USA) is mixed with equal amount of sodium carbonate (Na_2CO_3) followed by mechanical grinding and directly activated at higher temperatures in an electric furnace with the flowing of N_2 gas. Further, the activated ZrC is treated with 56 g concentrated HCl for 2 h in order to remove Na metal. The detailed procedure is presented in Scheme 1. Activated ZrC sample has been used in all the experiments reported in this study.

2.2. Preparation of Pt/ZrC-C electrocatalysts

The activated ZrC was incorporated over Vulcan carbon by solid-state reaction under intermittent microwave heating (IMH) method [33–35]. Typically, 0.02 g of activated ZrC was well dispersed over 0.02 g of Vulcan carbon XC-72R (C, Cabot Corp., $S_{BET} = 250\,m^2\,g^{-1}$) using 2-propanol as solvent by ultrasonic treatment for 15 min and the mixture was dried in an oven at 80 °C. It was then introduced into a microwave oven (Sharp NN-S327 WF, 2450 MHz, and 1100 W) and heated in six cycles, each cycle microwave treated for 20 s with a pause of 60 s between heating cycles. In a second step, platinum was loaded on ZrC-C composites by modified microwave-assisted polyol process, originally developed by Yu et al. [36]. Typically 0.5 mL of 0.1 mol L^{-1} $H_2PtCl_6\cdot6H_2O$ (Aldrich, ACS Reagent) was mixed with 25 mL of ethylene glycol (AR grade) in 100 mL beaker. 0.4 mol L^{-1} KOH (in ethylene glycol) was added drop wise to adjust the solution pH to about 10 in order to induce the formation of small and uniform Pt nanoparticles. This mixture was sonicated after adding 0.04 g of ZrC-C composites in

order to prepare Pt/ZrC-C electrocatalysts and the mixtures were again subjected to microwave irradiation for 50 s. The resulting suspension was filtered and the residue was washed with acetone and dried at 35 °C in a vacuum oven overnight. For comparative studies, commercial Pt/C catalyst (Johnson Matthey) has been employed.

2.3. Physical characterization

The phases and lattice parameters of the composite catalysts were characterized by powder X-ray diffraction (PXRD) employing Bruker AXS D8 diffractometer with Cu Kα radiation ($\lambda = 0.15418$ nm) operating at 40 kV and 30 mA. Nitrogen adsorption and desorption experiments were carried out by employing Micromeritics ASAP 2020 analyzer. The sample was outgassed at 100 °C for 2 h, followed by 150 °C for 10 h in dynamic vacuum before physisorption measurements. The specific surface area was calculated using the Brunauer–Emmett–Teller (BET) method, and the porosity distribution (0.2–20 nm) was generated from desorption branch of the isotherm by the Barrett–Joyner–Halenda (BJH) analysis. Scanning electron microscopy pictures were taken using a FEI Quanta 200 microscope. The sample powders were deposited on a carbon tape before mounting on the sample holder. X-ray photoelectron spectroscopy (XPS) measurements were performed on Omicron Nanotechnology spectrometer with Mg Kα monochromatic source operating at 15 kV and 20 mA. The spectra were recorded using 20 eV analyzer pass energy. High-resolution TEM (HRTEM) characterization was performed with a JEOL JEM-3010 transmission electron microscopy operated at 200 kV. Samples for HRTEM analysis were prepared by drying the nanocrystal dispersion in acetone on amorphous carbon coated copper grids.

2.4. Electrochemical characterization

The working electrodes for electrochemical measurements were fabricated by dispersing Pt/C or Pt/ZrC-C powders in 0.860 mL

ZrC (3 g) + Na$_2$CO$_3$ (3.0 g)
↓
Mechanical grinding and transferred 6 g mixture into an alumina boat
↓
The sample is placed in a tubular furnace and N$_2$ environment is maintained
↓
Temperature of the furnace is raised to 800 °C and the sample is kept at that temperature for 2 h
↓
The sample is weighed and was found to be 5.6 g. Then treated with 56 g HCl (conc.) for 2 h
↓
Filtered and washed with excess distilled water
↓
Dried in an oven at 150 °C for 2 h
↓
Activated ZrC (activated with Na$_2$CO$_3$)

Scheme 1. Systematic procedure adopted for ZrC activation.

of distilled water and 0.04 mL of 5 wt% nafion. Ultrasonic treatment was given for 15 min to achieve uniform dispersion of the mixture at room temperature. A known amount of suspension was deposited on the surface of a glassy carbon disk electrode (area = 0.164 cm^2) of RRDE (Pine Research Instruments) and the solvent was slowly evaporated. The Pt loadings on electrodes are normally controlled at 82 μg cm^{-2}. Electrochemical measurements were carried out in a conventional three electrode cell by using CHI 7081 C electrochemical workstation. The RRDE system consisted of a PINE rotator and an interchangeable electrode (E7 Series RRDE Tip). A platinum foil and saturated calomel electrode were used as counter and reference electrodes respectively. However, all potentials are quoted with respect to a reversible hydrogen electrode (RHE). The test solution consists of 0.1 mol L^{-1} HClO$_4$ as an electrolyte. The solutions were prepared using deionized water (Millipore, 18 MΩ cm). The dissolved oxygen was removed by purging the solution with pure argon for 30 min before starting the electrochemical experiments. In the ring disk measurements, the ring electrode was biased at 1.2 V (vs RHE) to maintain the peroxide oxidation reaction under pure diffusion control. The rotation rates were 400, 900, 1600 and 2500 rpm and the ORR polarization curves were recorded by scanning the potential from +1.0 V to +0.2 V (vs RHE) at 20 mV s^{-1}. Before each ORR measurement, the solution was purged with high pure O$_2$ gas for at least 40 min to ensure the oxygen saturation.

3. Result and discussion

3.1. Microstructure studies of activated ZrC

Fig. 1 shows powder XRD patterns of ZrC samples before and after Na$_2$CO$_3$ activation. For both the samples the main peaks are indexed at 2θ = 32.9° (1 1 1), 38.2° (2 0 0), 55.3° (2 2 0), 66.0° (3 1 1), 69.3° (2 2 2) and 82.1° (4 0 0) reflections, which agree well with standard powder diffraction patterns of face centered cubic structure of ZrC. No impurities related to the activating agent Na$_2$CO$_3$ are detectable. This indicates that vigorous chemical treatment given by the Na$_2$CO$_3$ activation does not induce any significant structural or microstructural changes in activated ZrC phase.

The surface textural characteristics of ZrC powders before and after Na$_2$CO$_3$ activation were evaluated by BET analysis using nitrogen gas adsorption–desorption isotherms as shown in Fig. 2. The BET analysis shows that the isotherm of un-activated ZrC is flat with limited nitrogen adsorption indicating very less surface area (0.6 m^2 g^{-1}) and no pores present. On the other hand, Na$_2$CO$_3$ activated ZrC shows very high volume of nitrogen adsorption. For Na$_2$CO$_3$ activated ZrC, there is a gradual increase in N$_2$ uptake starting at about p/p_0 = 0.4 and extending almost up to p/p_0 = 0.99 and
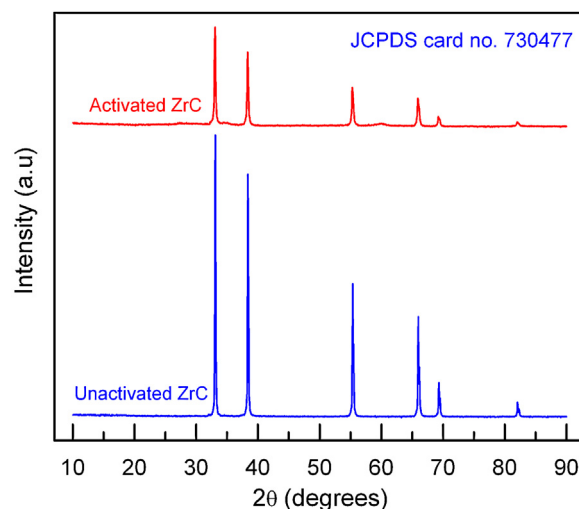

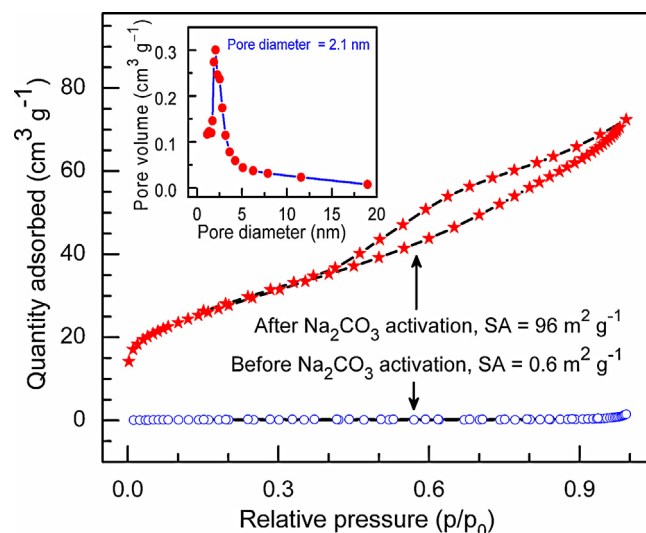**Fig. 1.** XRD pattern of ZrC before and after Na$_2$CO$_3$ activation.

Fig. 2. Nitrogen adsorption–desorption isotherms of ZrC before and after Na$_2$CO$_3$ activation. Inset shows pore size distribution of Na$_2$CO$_3$ activated ZrC calculated from the desorption branch of the isotherm using BJH method.

a steeper slope of the adsorption isotherm indicates high fraction of textural porosity. The isotherm has the characteristics of type IV with H3-type hysteresis behavior according to the IUPAC classification of physisorption isotherms [37]. The H3-type hysteresis is
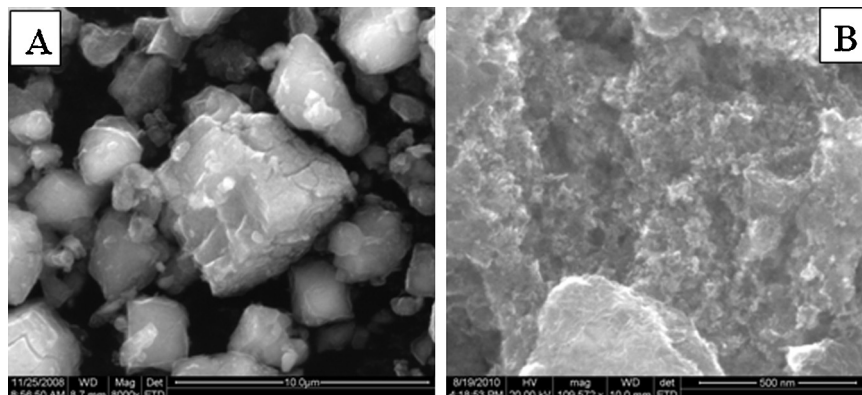

Fig. 3. SEM images of ZrC before (A), and after (B) Na$_2$CO$_3$ activation.

Before activation **After activation**

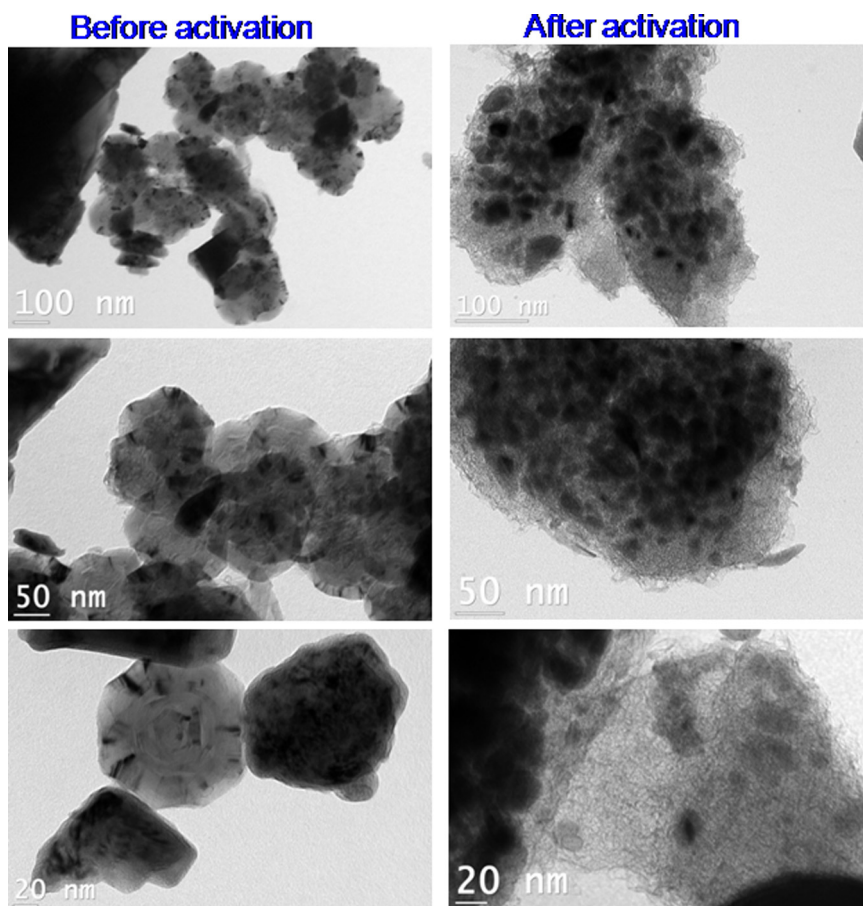**Fig. 4.** TEM images of ZrC before and after Na_2CO_3 activation with different magnifications.

usually generated due to slit-shaped pores. The BET surface area of activated ZrC powder is $96 \, m^2 \, g^{-1}$, which is much higher (about 160 times) than the unactivated ZrC powder ($0.6 \, m^2 \, g^{-1}$). The total pore volume of the activated ZrC powder is $0.112 \, cm^3 \, g^{-1}$. Na_2CO_3 activation adopted in this study predominately enhances the porous nature of ZrC with high surface area and large pore volume. This porous nature of activated ZrC can provide better electrochemical accessibility of the reactants. Chemical activation is a well-known method for preparing activated carbons which has been object of great study [38]. The alkali cations have a stronger role for the generation of pores on the activated carbons. It is reasonable to expect same mechanism for the generation of pores on the activated ZrC powders. The plot of pore size distribution determined by the BJH analysis shows the very narrow distribution of pores in the range of 2–4 nm with maxima at around 2.1 nm (inset of Fig. 2). The SEM images of the ZrC samples before and after Na_2CO_3 activation are shown in Fig. 3. The morphology of the unactivated ZrC is rock like structure without any significant pores. But after Na_2CO_3 activation, the pore skeleton of the sample is observed. The change in morphology and porosity has been confirmed by TEM study as shown in Fig. 4. The TEM pictures after Na_2CO_3 activation clearly show the porous nature of the activated ZrC. The porous nature of the activated ZrC is confirmed by BET analysis (Fig. 2). The microstructure studies give us a hint that the activated ZrC is a better material for fuel cell electrodes than unactivated ZrC.

3.2. Physical characterization of Pt/ZrC-C electrocatalyst

The powder XRD patterns of Vulcan carbon XC-72R (-C), ZrC, ZrC-C and Pt/ZrC-C catalysts are shown in Fig. 5. The broad diffraction peak at 24.5° is due to the (0 0 2) reflection of hexagonal Vulcan carbon XC-72R [9]. The fcc cubic ZrC is confirmed again with reflections that match well to those reported in JCPDS card no. 730477. The ZrC-C composite exhibit characteristic XRD peaks corresponding to both Vulcan carbons XC-72R and ZrC fcc phase. The Pt/ZrC-C catalyst shows broad peaks corresponding to reflections at $2\theta = 39.7°$ (1 1 1) and 46.4° (2 0 0), in addition to the reflections from ZrC and carbon. These reflections confirm the presence of fcc Pt
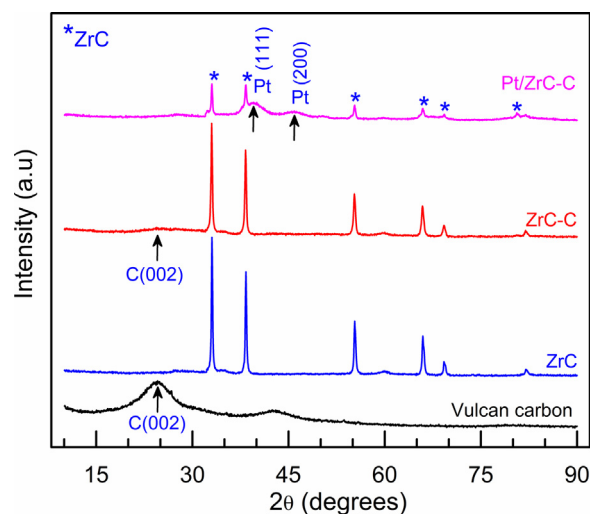

Fig. 5. Powder XRD pattern of Vulcan carbon XC-72R, ZrC, ZrC-C and Pt/ZrC-C electrocatalysts.
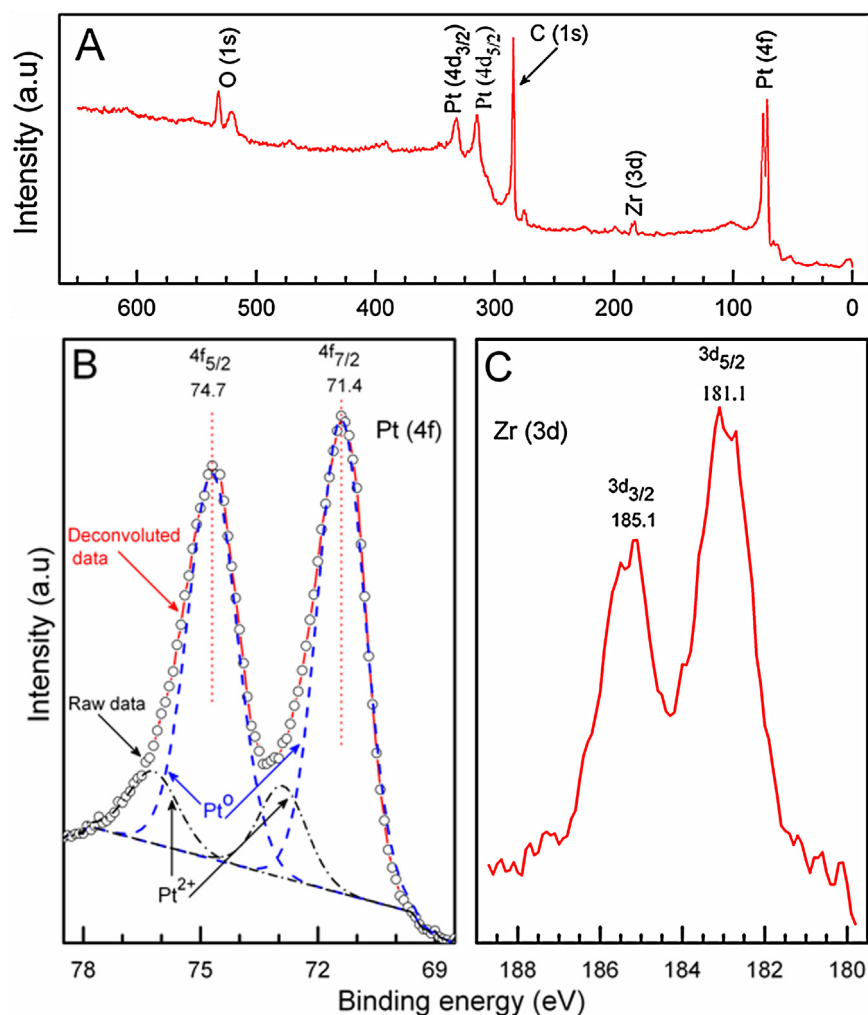
Fig. 6. Photoemission spectra of Pt/ZrC–C composites, (A) full scan of the catalyst, (B) Pt 4f spectrum, (C) Zr 3d spectrum.

crystallites on ZrC–C matrix [9]. The small remnant shoulders before 33° and 38.2° of Pt/ZrC–C are attributed to some elusive impurities of oxides/carbides. It is believed that Pt particles are interacting with each other on Vulcan carbon XC-72R and ZrC such interaction can modify the electroadsorption behavior.

Fig. 6A shows the photoemission survey spectrum of Pt/ZrC–C composite. Besides to the C 1s signal at 284.7 eV and O 1s at 532.5 eV, the Pt 4f, Pt 4d and Zr 3d signals appeared in the spectrum. The Pt 4f region (Fig. 6B) displays the spin-orbit splitting doublet peaks of $4f_{7/2}$ and $4f_{5/2}$ [14,39]. Deconvolution of Pt 4f region shows the presence of two pairs of doublets with theoretical peak area ratio of 57:43. The more intense doublet peaks at 71.4 and 74.7 eV are attributed to metallic Pt. The second and weaker doublet at 72.9 and 76.3 eV with higher binding energy (BE) of 1.5 eV than that of Pt^0 could be assigned to Pt^{2+} species due to surface oxide/hydroxide [14,23,40,41]. The relative area of integrated peak intensities of Pt^0 peak is 91% higher than that of Pt^{2+} species (9%) which is better than the reported ratio in the literature [14,40,41]. The XPS analysis of Pt/ZrC–C composites in the Zr 3d region is presented in Fig. 6C. A pair of peaks due to the Zr 3d core level split is observed at binding energies of 185.1 and 183.1 eV which correspond to the +4 ionic state of zirconium in the Pt/ZrC–C composites. The $3d_{5/2}$–$3d_{3/2}$ doublet peak is separated by 2.0 eV due to the spin–orbit coupling. These values confirm the presence of Zr^{4+} ionic state and correspond to the zirconium carbide. The XRD and XPS results confirm that there is an active interface between embedded Pt particles and ZrC support in the Pt/ZrC–C composites.

Transmission electron microscopy (TEM) images of Pt/ZrC–C with different magnifications were shown in Fig. 7. The Pt particles are homogeneously distributed on ZrC–C matrix. The images clearly reveal the spherical shaped Pt metal particles (dark spots) of about 2.6 nm sizes embedded on ZrC–C support. Similar images are reported earlier for Pt loaded carbon catalysts [12,33–35]. Rapid heating by microwave accelerates the reduction of metal ions and the nucleation of metal particles in the presence of ethylene glycol, which act as a both solvent and reducing agent [36]. The homogeneous microwave heating of liquid samples has an advantage of reducing the temperature and concentration gradients in the reaction medium, providing uniform environment for the nucleation and growth of the metal nanoparticles [36].

3.3. Electrochemical studies on pt/ZrC–C electrocatalyst

3.3.1. Cyclic voltammetry

The cyclic voltammograms of Pt/C and Pt/ZrC–C electrodes in 0.1 mol L^{-1} $HClO_4$ solution at a scan rate of 10 mV s^{-1} are shown in Fig. 8. The well-defined peaks for hydrogen adsorption/desorption ($0.0 V \leq E \leq 0.3 V$), the double layer potential plateau (0.3–0.5 V), and the peaks due to the formation (0.7–1.2 V) and reduction (1.2–0.45 V) of platinum surface oxides are clearly observed [13,14,28,42]. The shape of the cyclic voltammogram of these Pt nanocrystallites is different from that of the polycrystalline Pt [1] as a result of the higher double layer capacity due to the carbon support [43]. The currents resulting from double layer region
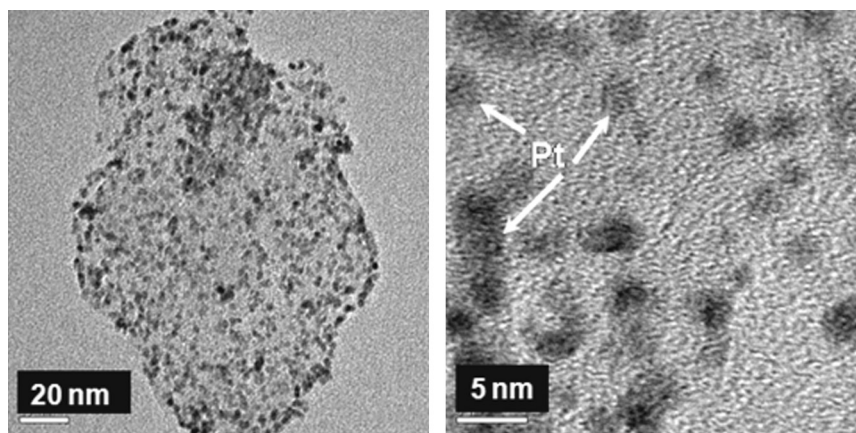
Fig. 7. TEM micrographs of the Pt/ZrC-C composites with different magnifications.

(∼0.3–0.5 V) of the CV curve on Pt/ZrC-C electrode are slightly lower than those on Pt/C electrode. This means that the Pt/C catalyst has higher surface area than the Pt/ZrC-C catalyst. This is because the surface area of Vulcan carbon XC-72 R (250 m^2 g^{-1}) is much higher than the activated ZrC (96 m^2 g^{-1}). Similar observation has also been made in number of cases of high surface area carbons [3,11,13,23]. The two hydrogen adsorption/desorption peaks at ∼0.07 and ∼0.13 V represents to the (1 1 0) and (1 0 0) facets of Pt [42,43]. The currents resulting from hydrogen adsorption and desorption on Pt/ZrC-C electrode are higher than those on Pt/C electrode. And also, the reduction peak for platinum oxide of Pt/ZrC-C electrode shifts toward positive potential direction of almost ∼70 mV. From Fig. 8, it is also evident that the Pt/ZrC-C electrode shows much larger oxide reduction peak current and hydrogen desorption area than Pt/C. This suggests that the combination of Pt and activated ZrC enhances the electrochemical active surface area as well as the activity for surface oxide formation and its reduction.

The cyclic voltammograms profiles corresponding to 1, 4, 10, 25, 50 and 70th cycles of Pt/ZrC-C electrocatalyst in 0.1 mol L^{-1} HClO$_4$ electrolyte are shown in Fig. 9. During the first scan, the anodic peak above 0.8 V can be attributed to the formation of platinum oxide. In the subsequent scans, the platinum oxide peak gradually decreases and stabilizes from 25th cycle onwards suggesting the formation of stable Pt surface. The current resulting from surface oxide formation/reduction at the subsequent cycles remained almost the same, highlighting the stability of the Pt/ZrC-C electrocatalyst after 25th cycles. The PtO reduction peak gradually

increases and stabilizes from 25th cycle onwards suggesting the formation of stable Pt surface. This observation is consistent with the literature reports on Pd-Pt bimetallic nanodendrites [23] and Pt-W$_2$C/C catalysts [30]. Meanwhile, the reduction peak for platinum oxide shifts slightly toward the positive potential direction and eventually stabilizes at ∼0.70 V. With increase in number of scans, the hydrogen region (0–0.3 V) gradualy evolves into a well-defined cyclic voltammetric profiles corresponding to hydrogen adsorption–desorption. The cyclic voltammograms profiles corresponding to various upper potential windows are displayed in Fig. 10. In the present work, the voltammetric profile corresponding to hydrogen adsorption/desorption is independent on the upper limit of the potential scan. But, at anodic potentials higher than +1.2 V, there is further oxidation on the Pt surface leading to higher valence oxides (a change from two to more than two electrons per Pt atom), as seen in Fig. 10. For this work, +1.2 V is chosen as an appropriate potential limit for all further electrochemical studies because up to +1.2 V the voltammetric profiles are stable without any unwanted anodic processes.

3.3.2. Rotating ring disk electrode (RRDE) measurements

Polarization curves of disk electrode (lower panel) and the fraction of current resulting from H$_2$O$_2$ production detected on ring electrode (upper panel) for the ORR on Pt/ZrC-C electrode in oxygen-saturated 0.1 mol L^{-1} HClO$_4$ at room temperature are shown in Fig. 11. The polarization curves have two
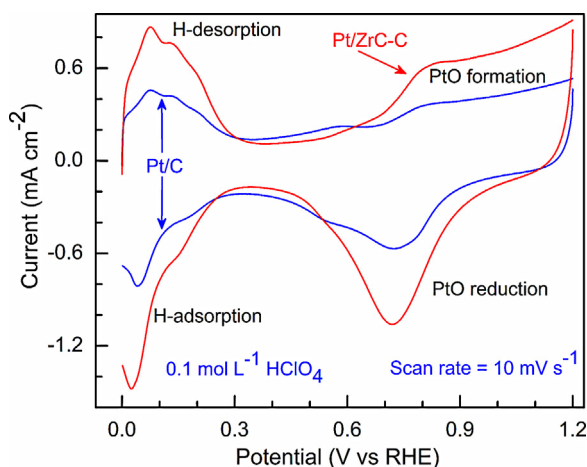

Fig. 8. The hydrogen electroadsorption voltammetric profiles of Pt/C and Pt/ZrC-C electrodes in N$_2$ saturated solution of 0.1 mol L^{-1} HClO$_4$.
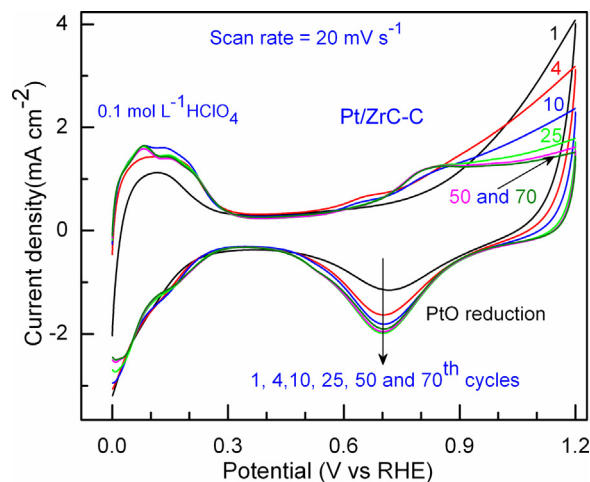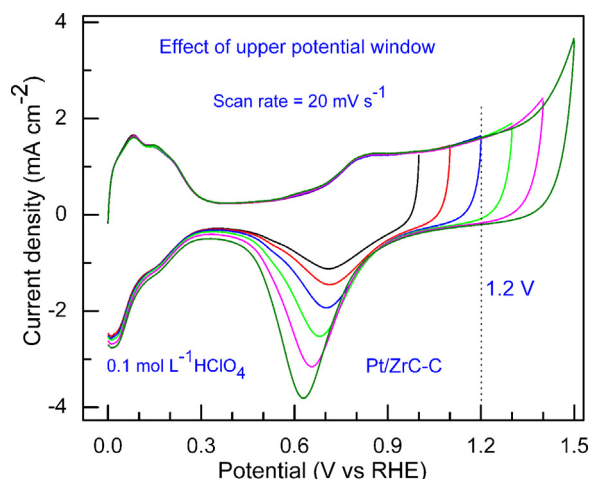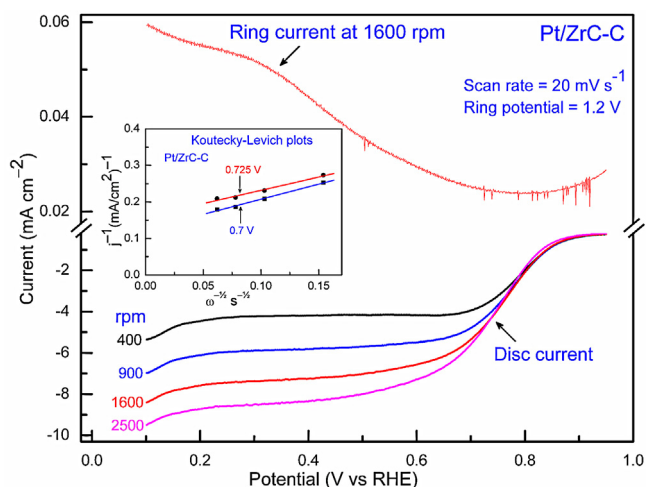

Fig. 9. Cyclic voltammogram profiles corresponding to 1, 4, 10, 25, 50 and 70th cycles of Pt/ZrC-C electrocatalyst in 0.1 mol L^{-1} HClO$_4$ electrolyte.
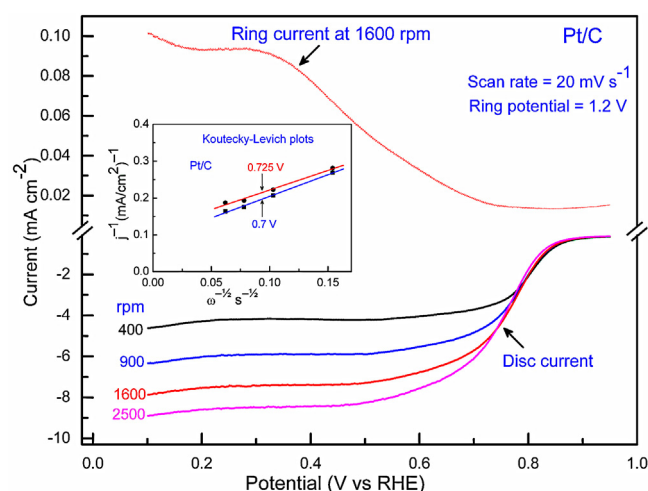
Fig. 10. Successive cyclic voltammogram profiles of Pt/ZrC-C electrocatalyst at various upper potential windows.

characteristic regions. The well-defined limiting current region (0.2–0.7 V) and the mixed diffusion-kinetic control region (0.7–0.95 V) are observed. The inset shows the Koutecky–Levich plot, whose linearity and parallelism suggest first-order kinetics with respect to molecular oxygen kinetics. From the slope of the straight lines (inset of Fig. 11), the B value for Pt/ZrC-C electrode is obtained as $1.294 \text{ mA s}^{-1/2}$. This B-factor is directly proportional to the number of electrons involved in the ORR [3,14]. Similarly, the polarization curves of disk electrode (lower panel) and the fraction of current resulting from H_2O_2 production detected on ring electrode (upper panel) for the ORR on Pt/C electrode in oxygen-saturated 0.1 mol L^{-1} $HClO_4$ at room temperature are shown in Fig. 12. The inset shows the Koutecky–Levich plot and the B-factor for Pt/C electrode is found to be $0.897 \text{ mA s}^{-1/2}$. This B value is smaller than that of Pt/ZrC-C electrode, which essentially means that the Pt/ZrC-C electrode has higher number of electrons transfered in ORR kinetics. The percentage of the current associated

Fig. 11. Polarization curves of glassy carbon disk electrode (lower panel) and the fraction of current resulting from H_2O_2 production detected on the Pt ring electrode (upper panel) for the ORR on Pt/ZrC-C electrode in oxygen-saturated 0.1 mol L^{-1} $HClO_4$ at room temperature. Ring potential = 1.2 V; ring and disk areas are 0.164 and 0.0365 cm^2 respectively; collection efficiency, N = 0.22; Pt loading = 82 $\mu g \, cm^{-2}$. Inset shows the Koutecky–Levich plot at various potentials.

Fig. 12. Polarization curves of glassy carbobn disk electrode (lower panel) and fraction of current resulting from H_2O_2 production detected on Pt ring electrode (upper panel) for the ORR on Pt/C electrode in oxygen-saturated 0.1 mol L^{-1} $HClO_4$ at room temperature. Ring potential = 1.2 V; ring and disk areas are 0.164 and 0.0365 cm^2 respectively; collection efficiency, N = 0.22; Pt loading = 82 $\mu g \, cm^{-2}$. Inset shows the Koutecky–Levich plot at various potentials.

Table 1
Surface area of ZrC, and ORR characteristics of Pt/C and Pt/activated ZrC-C electrodes.

Sample	Surface area ($m^2 \, g^{-1}$)	B-factor ($mA \, s^{-1/2}$)	% H_2O_2 at Pt ring
(0.4 V vs RHE)			
Unactivated ZrC	0.6	–	–
Activated ZrC	96	–	–
Pt/C	–	0.897	9.6
Pt/activated-ZrC-C	–	1.294	5.5

with peroxide generation at 0.4 V vs RHE is determined by using following equation [2]

$$\%H_2O_2 = \frac{2i_R/N}{i_D + i_R/N} \times 100,$$

where i_D is the disk current, i_R is the ring current, N is the collection efficiency of ring electrode (N = 0.22, provided by electrode manufacturer, Pine Research, USA) and are found to be 9.6% and 5.5% for Pt/C and Pt/ZrC-C electrodes respectively. The Pt/ZrC-C electrode performs better in terms of H_2O_2 formation than recently reported N-doped carbon materials [44]. The electron transfer number (n) was determined for Pt/ZrC-C electrode using the formula,

$$n = 4 - 2\left(\frac{i_R}{(i_D \times N)}\right)$$

and found to be ∼4 over the potential range from 0.7 to 0.9 V vs RHE. Therefore it confirms that Pt/ZrC-C electrode shows better performance than Pt/C for ORR activity. The main results of this study are summarized in Table 1.

4. Summary

Sodium carbonate activation method has been used to prepare porous ZrC from commercial ZrC. This method allows us to tune the microtextural properties, which include the specific surface area, pore volume, and pore dimension and distribution. As a result of sodium carbonate activation, there is tremendous increase in surface area of commercial zirconium carbide by about 160 times. The activated ZrC has been incorporated on Vulcan carbon XC-72R by a novel low-cost, reproducible, intermittent microwave heating (IMH) method and Pt^0 with particle size in the nanoscale

range of about 2.6 nm are loaded on ZrC-C composites by modified microwave-assisted polyol process. The voltammetric profile corresponding to hydrogen adsorption/desorption is independent on the upper limit of the potential scan. The resulted composite electrocatalyst showed higher ORR activity compared to the commercial Pt/C catalyst with similar metal loading. The approach described in this study is suitable for the activation of metal carbides, thus opening the door to develop porous metal carbides. This study also points out the dual role of ZrC as a support to Pt particles and promoter of ORR activity.

Acknowledgements

References

[1] N. Alonso-Vante, H. Tributsch, O. Solorza-Feria, Electrochim. Acta 40 (1995) 567–576.
[2] U.A. Paulus, T.J. Schmidt, H.A. Gasteiger, R.J. Behm, J. Electroanal. Chem. 495 (2001) 134–145.
[3] U.A. Paulus, A. Wokaun, G.G. Scherer, T.J. Schmidt, V. Stamenkovic, V.N. Radmilovic, M. Markovic, P.N. Ross, J. Phys. Chem. B 106 (2002) 4181–4191.
[4] A. Brouzgou, S.Q. Song, P. Tsiakaras, Appl. Catal. B: Environ. 127 (2012) 371–388.
[5] Y. Wang, P.B. Balbuena, J. Phys. Chem. B 109 (2005) 18902–18906.
[6] J.L. Fernández, V. Raghuveer, A. Manthiram, A.J. Bard, J. Am. Chem. Soc. 127 (2005) 13100–13101.
[7] R. Bashyam, P. Zelenay, Nature 443 (2006) 63–66.
[8] J. Greeley, I.E.L. Stephens, A.S. Bondarenko, T.P. Johansson, H.A. Hansen, T.F. Jaramillo, J. Rossmeisl, I. Chorkendorff, J.K. Nørskov, Nat. Chem. 1 (2009) 552–556.
[9] E. Antolini, R.R. Passos, E.A. Ticianelli, Electrochim. Acta 48 (2002) 263–270.
[10] J. Xie, D.L. Wood, K.L. More, P. Atanassov, R.L. Borup, J. Electrochem. Soc. 152 (2005) A1011–A1020.
[11] H. Yang, N. Alonso-Vante, J.-M. Léger, C. Lamy, J. Phys. Chem. B 108 (2004) 1938–1947.
[12] A.R. Malheiro, J. Perez, H.M. Villullas, J. Power Sources 195 (2010) 3111–3118.
[13] H.A. Gasteiger, S.S. Kocha, B. Sompalli, F.T. Wagner, Appl. Catal. B: Environ. 56 (2005) 9–35.
[14] P. Hernández-Fernández, S. Rojas, P. Ocón, J.L.G. de la Fuente, P. Terreros, M.A. Peña, J.L. García-Fierro, Appl. Catal. B: Environ. 77 (2007) 19–28.
[15] V. Stamenković, T.J. Schmidt, P.N. Ross, N.M. Marković, J. Electroanal. Chem. 554–555 (2003) 191–199.
[16] R. Yang, J. Leisch, P. Strasser, M.F. Toney, Chem. Mater. 22 (2010) 4712–4720.
[17] S. Song, Y. Wang, P. Tsiakaras, P.K. Shen, Appl. Catal. B: Environ. 78 (2008) 381–387.
[18] S.-J. Liu, C.-H. Huang, C.-K. Huang, W.-S. Hwang, Chem. Commun. (32) (2009) 4809–4811.
[19] H. Liu, W. Li, A. Manthiram, Appl. Catal. B: Environ. 90 (2009) 184–194.
[20] N.N. Kariuki, X. Wang, J.R. Mawdsley, M.S. Ferrandon, S.G. Niyogi, J.T. Vaughey, D.J. Myers, Chem. Mater. 22 (2010) 4144–4152.
[21] A. Sarkar, A.V. Murugan, A. Manthiram, J. Mater. Chem. 19 (2009) 159–165.
[22] M.H. Shao, T. Huang, P. Liu, J. Zhang, K. Sasaki, M.B. Vukmirovic, R.R. Adzic, Langmuir 22 (2006) 10409–10415.
[23] B. Lim, M. Jiang, P.H.C. Camargo, E.C. Cho, J. Tao, X. Lu, Y. Zhu, Y. Xia, Science 324 (2009) 1302–1305.
[24] B. Wang, J. Power Sources 152 (2005) 1–15.
[25] R. Kothandaraman, V. Nallathambi, K. Artyushkova, S.C. Barton, Appl. Catal. B: Environ. 92 (2009) 209–216.
[26] T.J. Schmidt, U.A. Paulus, H.A. Gasteiger, N. Alonso-Vante, R.J. Behm, J. Electrochem. Soc. 147 (2000) 2620–2624.
[27] N. Alonso-Vante, I.V. Malakhov, S.G. Nikitenko, E.R. Savinova, D.I. Kochubey, Electrochim. Acta 47 (2002) 3807–3814.
[28] H. Meng, P.K. Shen, J. Phys. Chem. B 109 (2005) 22705–22709.
[29] Y. Wang, S. Song, V. Maragou, P.K. Shen, P. Tsiakaras, Appl. Catal. B: Environ. 89 (2009) 223–228.
[30] N.R. Elezovic, B.M. Babic, P. Ercius, V.R. Radmilovic, L.M. Vracar, N.V. Krstajic, Appl. Catal. B: Environ. 125 (2012) 390–397.
[31] V. Kiran, K. Srinivasu, S. Sampath, Phys. Chem. Chem. Phys. 15 (2013) 8744–8751.
[32] S. Yoshimoto, J. Inukai, A. Tada, T. Abe, T. Morimoto, A. Osuka, H. Furuta, K. Itaya, J. Phys. Chem. B 108 (2004) 1948–1954.
[33] P. Justin, G. Ranga Rao, Catal. Today 141 (2009) 138–143.
[34] P. Justin, P.H.K. Charan, G. Ranga Rao, Appl. Catal. B: Environ. 100 (2010) 510–515.
[35] P. Justin, G. Ranga Rao, Int. J. Hydrogen Energy 36 (2011) 5875–5884.
[36] W. Yu, W. Tu, H. Liu, Langmuir 15 (1999) 6–9.
[37] F. Rouquerol, J. Rouquerol, K. Sing, Adsorption by Powders and Porous Solids: Principles, Methodology and Applications, Academic Press, San Diego, 1999.
[38] K. Okada, N. Yamamoto, Y. Kameshima, A. Yasumori, J. Colloid Interface Sci. 262 (2003) 179–193.
[39] S. Hüfner, Photoelectron Spectroscopy: Principles, Applications, Springer, Berlin, 1996.
[40] F. Liu, J.Y. Lee, W.J. Zhou, Adv. Funct. Mater. 15 (2005) 1459–1464.
[41] N.-Y. Hsu, C.-C. Chien, K.-T. Jeng, Appl. Catal. B: Environ. 84 (2008) 196–203.
[42] S. Kinge, C. Urgeghe, A. De Battisti, H. Bönnemann, Appl. Organomet. Chem. 22 (2008) 49–54.
[43] S.K. Meher, G. Ranga Rao, ACS Catal. 2 (2012) 2795–2809.
[44] C.H. Choi, S.H. Park, S.I. Woo, Appl. Catal. B: Environ. 119–120 (2012) 123–131.